Durham University

DEPARTMENT OF PHYSICS

MPHYS THEORETICAL PHYSICS: LEVEL 4 PROJECT

April 18, 2018

Calculating the Charge Asymmetry in Top-quark Pair Production

Author:
Chiho So

Supervisor:
Dr. Ben Pecjak

Abstract

There is a large discrepancy between the measured charge asymmetry at the Tevatron and the theoretical predictions from the Standard Model for top quark pair production. This asymmetry arises from a difference in the production rates of top and antitop quarks in the forward hemisphere. In this work, a parton-level Monte Carlo event generator is constructed to directly compute the charge asymmetry for the Tevatron and at the Large Hadron Collider (LHC), which is calculated at first non-vanishing order (α_s). For the Tevatron, an asymmetry of 4-5% is predicted in the lab frame and $\sim$ 7% in the $t\bar{t}$ frame which differs from the experimental result of 15% measured by CDF. At the LHC, cut-independent and cut-dependent asymmetries are introduced to study the asymmetry in suitable kinematic regions. Through these cuts the top quark is found to be predominantly produced at higher rapidities while the antitop is more centrally produced.

Contents

1 Introduction

The top quark is the heaviest known fundamental particle. It has a mass of approximately 170 MeV which is similar to that of a gold atom and yet it behaves as a single point-like particle. The top quark was first postulated in 1973 by Kobayashi and Maskawa [1] and discovered in 1995 by CDF [2] and DØ [3] experiments at the Tevatron through the collision of protons and antiprotons. Since then, top quark events have been abundant with 5 million top and antitop quark ($t\bar{t}$) pairs being produced at ATLAS and CMS during the LHC's Run 1 [4]. However, it is a highly unstable particle and unable to hadronize because of its short lifetime. Therefore, it is detected through its decay products which are almost exclusively bW^+[5].

1.1 Charge asymmetry

Top quark physics is now at the forefront of particle physics. It establishes itself as a useful probe for electroweak symmetry breaking due to its large mass being within the same magnitude as the electroweak scale [5]. A particularly interesting area of research is the charge asymmetry, which arises from a difference between the production rates of top quarks and antitop quarks produced in the forward hemisphere [15]. The asymmetry can be defined by

$$A_C^i = \frac{N(y_t^i > 0) - N(y_{\bar{t}}^i > 0)}{N(y_t^i > 0) + N(y_{\bar{t}}^i > 0)} = \frac{\sigma(y_t^i > 0) - \sigma(y_{\bar{t}}^i > 0)}{\sigma(y_t^i > 0) + \sigma(y_{\bar{t}}^i > 0)} \equiv \frac{\sigma_A^i}{\sigma_S^i}, \tag{1}$$

where i denotes the Lorentz frame, which are mainly the center-of-mass frame of the top-quark pair ($t\bar{t}$ frame), or in the laboratory frame. In the case of the Tevatron, the laboratory frame is the $p\bar{p}$ frame while for the LHC it is the pp frame. The N denotes the number of events which is convenient for experimental measurements. However, in theoretical calculations, the equation is written in terms of cross sections. From Equation 1, one can see that integrating rapidity distributions over the appropriate regions results in an asymmetry given by the asymmetric (σ_A) and symmetric (σ_S) cross section [15]. The equation for rapidity is given by

$$y = \frac{1}{2} \ln \left(\frac{E + p_z}{E - p_z} \right), \tag{2}$$

where E is the energy of the particle and p_z is the longitudal momentum along the z-axis or beam axis [7]. The asymmetry can be defined in terms of the angle between the outgoing particle and beam axis, θ, but it is more conventional to use the rapidity as rapidity differences are Lorentz boost invariant.

In the case of a $p\bar{p}$ collider such as the Tevatron, the charge asymmetry is unique in that it can be measured instead as a forward-backward (FB) asymmetry. This follows from charge conjugation invariance, where particles are exchanged for their antiparticles, which implies that $N(y_t^i > 0) = N(y_t^i < 0)$ [8]. Hence, the FB asymmetry can be defined as

$$A_{FB}^i = \frac{N(y_t^i > 0) - N(y_t^i < 0)}{N(y_t^i > 0) + N(y_t^i < 0)} = \frac{\sigma(y_t > 0) - \sigma(y_t < 0)}{\sigma(y_t > 0) + \sigma(y_t < 0)} \equiv \frac{\sigma_A^i}{\sigma_S^i}, \qquad (3)$$

where the asymmetry arises from differences in the production rate of top quarks in the forward and backward hemispheres.

For a pp collider such as the LHC, due to the initial symmetric state, we infer that the rapidity distributions of the top and antitop quarks are also symmetric and hence, is charge symmetric in the laboratory frame [8]. However, at given rapidities, the rates differ and so cuts can be imposed to study the asymmetry in kinematic regions where it is most prominent.

1.2   Project Aims

The aim of this project is to build a parton-level Monte Carlo (MC) program to measure the charge asymmetry in top quark pair production. While there are already MC programs capable of calculating cross sections at next-to-leading order, such as Madgraph [9], the asymmetric contributions will be addressed directly allowing for a more efficient calculation of the charge asymmetry. The main motivation behind this project arises from the discrepancy between the experimental measurements at the Tevatron and the theoretical predictions provided by the Standard Model (SM). While the precision of the measurement at the Tevatron is hindered by the small sample size of top quarks produced, the difference between theory and experiment could be due to production mechanisms from physics beyond the SM [5].

The project first begins by explaining the MC integration method and how it can be utilised for event generation. The accuracy of the MC program is demonstrated on a simpler leptonic process, $e^+e^- \rightarrow Z/\gamma \rightarrow \mu^+\mu^-$, which has an analytical solution. Next, the theory behind $t\bar{t}$ production is explained. This will include the leading-order (LO) QCD contributions at $\mathcal{O}(\alpha_s^2)$ as well as next-to-leading order (NLO) QCD asymmetric contributions at $\mathcal{O}(\alpha_s^3)$. The 'phase-space slicing method' is implemented in order to integrate the higher order corrections. Next, these tools will be used to calculate values for the FB asymmetry and produce distributions at the Tevatron, which will be compared to experimental data as well as SM predictions from other work [10][21]. The adaptations needed to measure the charge asymmetry at the LHC are discussed and the results are presented and compared to experimental data and SM predictions from [23]. In both of

these sections, the parameters used are highlighted so others may reproduce our work. As discussed in chapter 4, the charge asymmetry is calculated at first non-vanishing order (α_s), which is referred to as NLO [10]. It is important to note that a next-to-next-to-leading order (NNLO) QCD calculation has been computed for the charge asymmetry, which also includes NLO electro-weak (EW) corrections at $\mathcal{O}(\alpha\alpha_s^2)$ [17]. However, the work in this project can serve as a template for which higher order corrections such as soft-gluon resummation or EW corrections may be added [10][15]. The calculations presented here are also relevant for $b\bar{b}$ pair production.

2   Monte Carlo

In this section the MC methods used to achieve the aim of this project are described. In section 2.1 the theory behind MC integration techniques and how they are used for event generation is discussed. In section 2.2 these methods are applied to a simpler process of $e^+e^- \to Z/\gamma \to \mu^+\mu^-$ and the results are compared to an analytical solution.

2.1   Monte Carlo Techniques

A MC program uses random sampling to obtain a numerical result. They are crucial tools for analysing and interpreting experimental data which allow us to make comparisons between theory and experiments. It has an advantage over other integration methods in that it has a fast convergence for high dimensional integrals. This feature is particularly relevant for particle physics as differential cross sections often involve multi-dimensional phase-space integrals. The other aspect that makes it appealing for particle physics is how it can be utilised for constructing event generators. This is due to the randomness of the numerical method being analogous to the random physical process. The benefit of generating events is that multiple observables can be binned simultaneously into histograms without analytically performing Jacobian transforms which can be mathematically arduous.

The basis of MC integration works on the simple observation that an integral can be recast as the average of the integrand, $\langle f(x) \rangle$, as shown below

$$I = \int_{x_1}^{x_2} f(x)dx = (x_2 - x_1)\langle f(x) \rangle. \tag{4}$$

Consequently, we can extend this concept to be more suitable for a computer program. This is achieved by approximating the integral as a sum evaluated from a random distri-

bution of N points within the range of (x_1, x_2) [6]. The sum is written as

$$I \approx I_N = (x_2 - x_1)\frac{1}{N}\sum_{n=1}^{N} f(x_i) = \frac{1}{N}\sum_{n=1}^{N} W_i,$$ (5)

where, for convenience, the integral is defined to be the average of the weight, $W_i = (x_2 - x_1)f(x_i)$. From Equation 5 it is evident that sampling from a larger distribution of N points produces a more accurate result.

The MC integration method is converted into an event generator by using a 'hit-or-miss' method. During the MC integration, the random points generated belong to the phase space of the integral. Each point represents a state of the system also known as an 'event'. The 'hit-or-miss' method aims to unweight the events by assigning a probability to the process, which is accomplished by performing the integration twice. During the first integration, the value for the integral is obtained along with the maximum weight, W_{max}. Each weight is proportional to the probability of it occurring and is given by W_i/W_{max}. For the second integration, the randomly chosen events can be 'accepted or 'rejected' based on if the probability is larger than a random number, $R \in (0,1)$. Events with a higher probability occur more frequently, while low probability events are suppressed. The process is continued until a desired number of events are generated. Binned events are then converted to a differential distribution through normalisation.

In this work, the VEGAS algorithm [11] is used, which is an adaptive multi-dimensional MC integration method. It is an iterative process which works by randomly sampling from a distribution that closely resembles the function being integrated. With each iteration, the MC adapts to concentrate on sampling in areas where the contribution to the integral is largest. This is a form of importance sampling in that a Jacobian transform is performed in an attempt to flatten the integral and improve its convergence.

2.2 A Simpler Process

A MC event generator was produced for the leptonic process, $e^+e^- \rightarrow Z/\gamma \rightarrow \mu^+\mu^-$, which has an analytical solution so the accuracy of the VEGAS integrator can be tested. This is also simpler than a hadronic process as the colliding leptons are elementary so the centre-of-mass energy is fixed. Beginning with this process allows us to build a good foundation to be expanded for top quark pair production. The details of the calculation can be found it [6], where Feynman diagrams are used to calculate scattering amplitudes resulting in a differential cross section given by

$$\frac{d\sigma}{d\Omega} = \frac{\alpha^2}{4\hat{s}}\left[A_0(1 + cos^2\theta) + A_1 cos\theta\right],$$ (6)

where $\alpha = e^2/(4\pi)$ is the QED running coupling and $d\Omega = dcos\theta d\phi$ is the phase factor. The first term in the brackets is given by the photon contribution, while the term linear in $cos\theta$ is generated by the Z boson. A_0 and A_1 are terms which depend on the coupling of fermions to Z bosons. Since the expression does not depend on the angle ϕ, it can be integrated over, which introduces a multiplicative factor of 2π. The overall result is a one dimensional integral in $cos\theta$, which has a non-trivial solution when integrated between the limits [1, -1]. The analytic result is

$$\sigma = \frac{4\pi\alpha^2}{3\hat{s}}A_0 = 1060.93 \; pb, \tag{7}$$

for a colliding centre of mass energy, $E_{cm} = 90 \; GeV$. Note that the Z contribution integrates to zero due to its asymmetry. The MC result agrees with the analytical solution
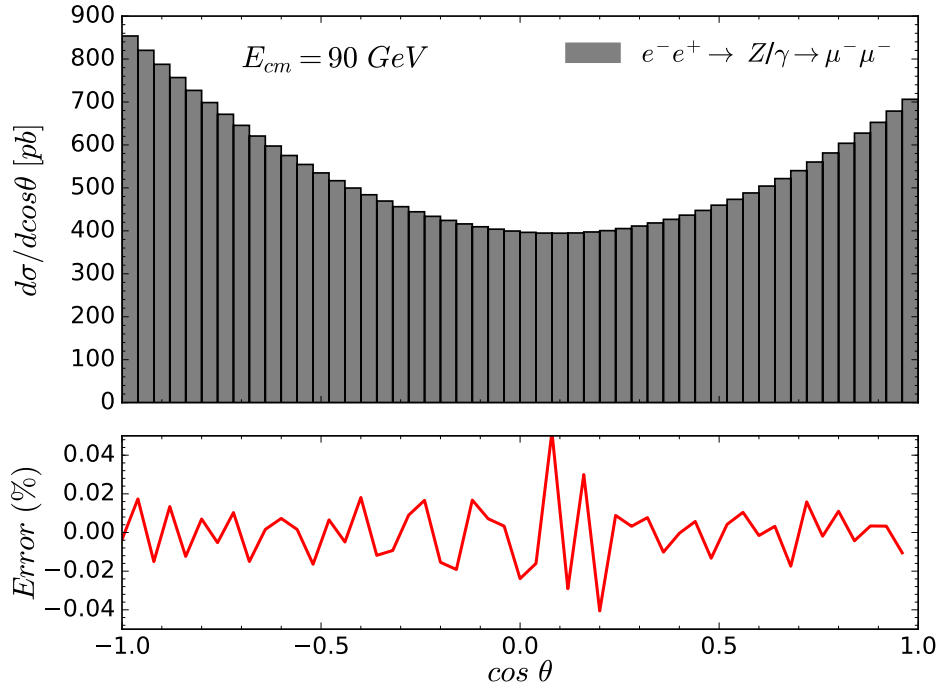

Figure 1: The differential cross section, $d\sigma/dcos\theta$, for the leptonic process $e^+e^- \rightarrow Z/\gamma \rightarrow \mu^+\mu^-$ at $E_{cm} = 90 \; GeV$ using the VEGAS integrator. The percentage error is provided for each bin.

in Equation 7. In Figure 1 the distribution for $cos\theta$ is plotted along with the percentage error in each bin, which is within $\pm0.05\%$. This shows that the VEGAS integrator provides sufficient numerical precision. For the NLO calculations in the top quark production, the integration error is larger due to higher dimensional phase-space integrals. However,

the error is insignificant when compared to the uncertainty that arises from varying the factorisation scale.

3 Top Quark Pair Production

In this section the main aim of the project is discussed, which is the production of on-shell $t\bar{t}$ pairs. In section 3.1 the basics of fixed-order calculations are introduced alongside the leading-order Feynman diagrams, which have a symmetric contribution to the cross section. The higher order asymmetric QCD corrections, from which the charge asymmetry originates, are presented in section 3.2. In section 3.3 the 'phase-space slicing method' is described. This method is applied for solving higher order QCD corrections using Monte-Carlo techniques.

3.1 Perturbative QCD and Leading Order Diagrams

In this section the production of on-shell $t\bar{t}$ pairs in a hadron collider is discussed. Thus, the hadronic scattering process being considered is

$$N_1(P_1) + N_2(P_2) \rightarrow t(P_3) + \bar{t}(P_4) + X, \tag{8}$$

where N_1 and N_2 represent incoming hadrons such as $p\bar{p}$ at the Tevatron or pp at the LHC and X are hadronic final states [15]. This process is more complicated than the electron-positron collision shown in section 2.2 as the colliding hadrons are not elementary particles. The collisions occur between their constituent partons, such as the valence quarks, gluons and sea quarks, resulting in a centre-of-mass energy which is variable. Additionally, the process requires Lorentz-boosts in order to construct observable distributions in the centre-of-mass or laboratory frames.

An arbitrary hadronic cross section is introduced, which is given in terms of partonic cross sections, convoluted with parton distribution functions (PDFs) that describe the the probability density for finding a particle with longitudinal momentum fraction, x_i. Note that the PDFs are not derived from perturbative QCD, but come from experimental data [14]. The hadronic cross section is written as

$$d\sigma = \sum_{ij} \int dx_1 dx_2 f_{i/N_1}(x_1, \mu_F) f_{j/N_2}(x_2, \mu_F) d\hat{\sigma}_{ij}(\hat{s}, \mu_F, \mu_R, \alpha_s(\mu_R)). \tag{9}$$

Non-perturbative collinear singularities are assumed to be factorised into the PDFs, $f_{i/N}$, which depend on a factorisation scale, μ_f [12]. The strong coupling constant, α_s, sets the

strength of interactions involving QCD and decreases with the renormalisation scale, μ_R [13]. The partonic centre-of-mass energy squared is given by $\hat{s} = x_1 x_2 S$ where S is the hadronic centre-of mass energy squared. The partonic cross section, $d\sigma_{ij}$, can be expanded in series of α_s

$$d\hat{\sigma}_{ij} = \alpha_s^2 \left[d\hat{\sigma}_{ij}^{(0)} + \frac{\alpha_s}{\pi} d\hat{\sigma}_{ij}^{(1)} + \frac{\alpha_s^2}{\pi^2} d\hat{\sigma}_{ij}^{(2)} ... \right], \tag{10}$$

where the first term in brackets is denoted as leading-order (LO), the second term as next-to-leading order (NLO), the third term as next-to-next-to-leading-order (NNLO), and so on [15]. Differential cross sections can then be calculated from Feynman diagrams using perturbative QCD.

In hadronic collisions, the main subprocess for producing top quark pairs is the strong interaction, namely through quark-antiquark annihilation and gluon fusion [15].

$$q(p_1) + \bar{q}(p_2) \rightarrow t(p_3) + \bar{t}(p_4), \tag{11}$$

$$g(p_1) + g(p_2) \rightarrow t(p_3) + \bar{t}(p_4). \tag{12}$$

These subprocesses are shown schematically in Figure 2 with quark-antiquark annihilation depictated in in Figure 2a and gluon fusion process shown in Figure 2b - d [4]. The Born level, or LO, differential cross sections for quark-antiquark annihilation and gluon-fusion are provided by [16] but shall be listed in the appendix (see appendix, Equation B.1 and Equation B.2), for the convenience of the reader. The LO cross sections only contain symmetric parts and hence the denominator for the charge asymmetry will be given by the Born cross section. As both LO reactions involve a one-dimensional integral over $cos\theta$, they are not computationally difficult to solve. The LO differential cross sections is applied to Equation 9 and the PDFs are adjusted for the appropriate hadron collider. The constraint, $\hat{s} > 4m_t^2$, is also imposed to ensure there is enough energy in the collision to produce a top and antitop quark of mass m_t.
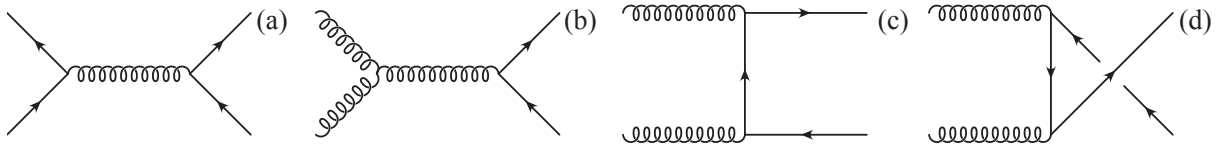

Figure 2: The leading order Feynman diagrams which contribute towards $t\bar{t}$ pair production.

3.2   Asymmetric QCD Corrections (NLO)

As discussed in section 3.1, the LO terms only have a symmetric contribution to the cross section and therefore don't contribute to the charge asymmetry. In order to investigate the charge asymmetry, the NLO QCD corrections have to be considered.

The dominant process which contributes to the asymmetry is $q\bar{q}$ annihilation. This asymmetry arises from interference between Born amplitudes for $q\bar{q} \to t\bar{t}$ (Figure 3d) and one-loop corrections (Figure 3c), known as virtual corrections, as well as interference terms between real gluon emission in initial and final states (Figure 3a-b). The other source of asymmetry originates from interference terms in heavy flavour production through quark-gluon scattering, as shown in Figure 4 [16]. Note that triple gluon coupling diagrams do not contribute as they have charge symmetric amplitudes. The two subprocesses for real gluon emission and quark-gluon scattering are

$$q(p_1) + \bar{q}(p_2) \to t(p_3) + \bar{t}(p_4) + g(p_5), \tag{13}$$

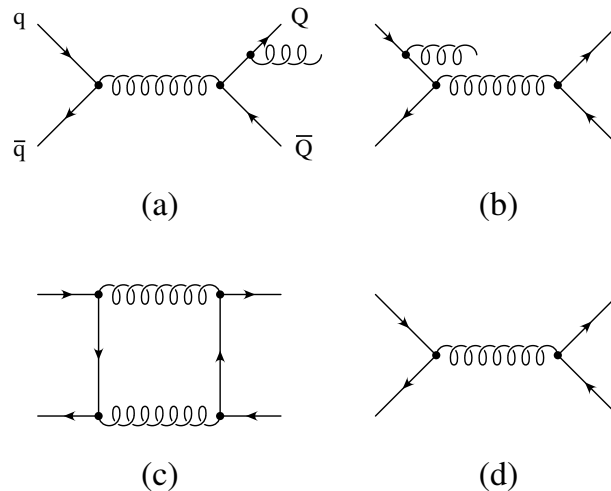$$q(p_1) + g(p_2) \to t(p_3) + \bar{t}(p_4) + q(p_5). \tag{14}$$

Figure 3: The charge asymmetry contribution from $q\bar{q}$ annihilation due to inteference of final state (a) with initial state (b) radiation and inteference of one loop box amplitude (c) with the Born diagram (d).

The one-loop diagram is ultraviolet finite in the high energy region, which means it does not exhibit a divergence [16]. This leads to the conclusion that no collinear singularities are present, where gluons are produced collinear to final state particles [18]. However, in the low energy region, virtual corrections and real radiation must be summed to compensate
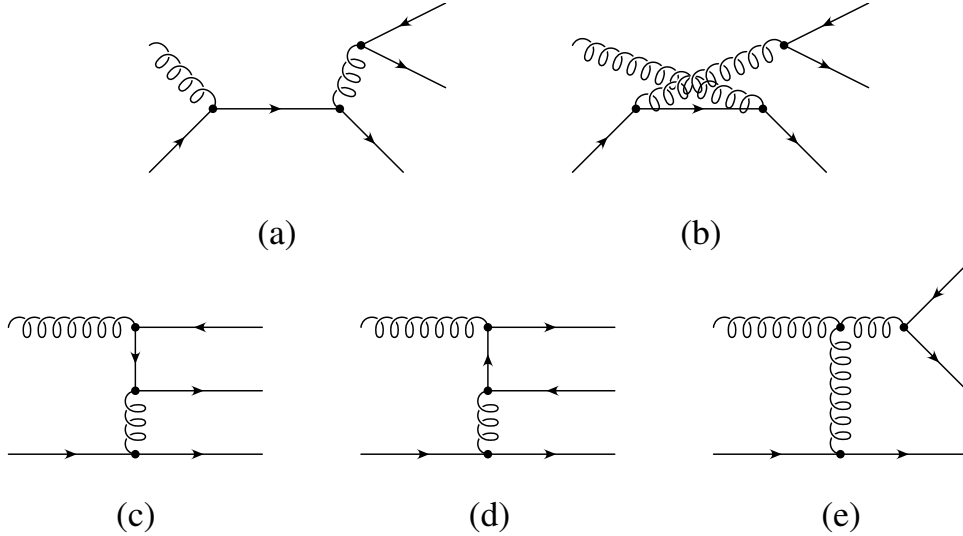
Figure 4: The charge asymmetry contributions from quark-gluon scattering.

for the infrared divergences. These infrared divergences are singularities that occur from integration momenta tending to zero in phase space integrals for one-loop diagrams and in real gluon emission (soft singularities). However, these divergent terms have opposing signs and precisely cancel upon addition [18]. The following section shows the 'phase-space slicing method', which must be employed to solve the QCD corrections in these two energy regions.

3.3   Phase-Space Slicing

The phase-space slicing method works by separating the phase-space into two regions, which are labeled as soft, S, and hard, H. This can be written as

$$\sigma = \frac{1}{2\Phi} \int \overline{\sum} |M_3|^2 d\Gamma_3 = \frac{1}{2\Phi} \int_S \overline{\sum} |M_3|^2 d\Gamma_3 + \frac{1}{2\Phi} \int_H \overline{\sum} |M_3|^2 d\Gamma_3, \tag{15}$$

where $\Phi = \lambda^{1/2}(\hat{s}, m_1^2, m_1^2)$ is the usual flux factor, which depends on the partonic centre-of-mass energy squared and the incident particle masses m_1 and m_2. The two-to-three body squared matrix, $\overline{\sum}|M_3|^2$, is summed over the final states, and $d\Gamma_3$ is the three-body phase space [19]. The soft region contains the infrared divergences mentioned in section 3.2.

The hard is partitioned from the soft by imposing a cutoff, E_{cut}, on the energy of the soft gluon. The soft region can then be defined by $0 \leq E_5 \leq E_{cut}$, and the hard region by $E_5 > E_{cut}$, where E_5 the gluon energy in the partonic rest frame. The cut on the soft

gluon is necessary to achieve a finite result, as it prevents the build up of arbitrarily large logarithms. Further, E_{cut} is approximated to be small so there is no dependence on its value [19].

For the soft calculation it can be shown that since $p_5^\mu \to 0$, the three body phase space can be simplified down to eikonal factors multiplied by the Born amplitude (Figure 3d) using the double pole approximation [19]. The NLO asymmetric differential cross sections are provided by [16] (see Appendix B). The equation for the soft region (Equation B.7) contains virtual and soft contributions. For the hard process (Equation B.5) we will only consider real gluon emission. The equation for quark-gluon scattering (Equation B.12) has been corrected to sum over quark and gluon colours. To be explicit, the asymmetric cross section involves integrating phase-space integrals of the form

$$\hat{\sigma}_A^{q\bar{q},virt+soft}(\hat{s}) = \int dcos\theta \; \frac{d\hat{\sigma}_A^{q\bar{q},virt+soft}}{dcos\theta}, \tag{16}$$

$$\hat{\sigma}_A^{q\bar{q},hard}(\hat{s}) = \int dcos\theta d\phi dy_{45} dy_{35} \; \frac{d\hat{\sigma}_A^{q\bar{q},hard}}{dy_{35} dy_{45} d\Omega}, \tag{17}$$

$$\hat{\sigma}_A^{q\bar{q}}(\hat{s}) = \hat{\sigma}_A^{q\bar{q},hard}(\hat{s}) + \hat{\sigma}_A^{q\bar{q},virt+soft}(\hat{s}), \tag{18}$$

for the quark-antiquark channel and

$$\hat{\sigma}_A^{qg}(\hat{s}) = \int dcos\theta d\phi dy_{45} dy_{35} \; \frac{d\hat{\sigma}_A^{qg}}{dy_{35} dy_{45} d\Omega}, \tag{19}$$

for the quark-gluon channel. Note that both the hard and quark-gluon integrals involve a four-dimensional phase-space that depends on y_{34}, y_{45} and $d\Omega = dcos\theta \; d\phi$. A parameterisation for the four-momentum vectors, $p_1...p_5$, must be chosen to find the integration limits for the phase space. In the case of hard process, the energy of the gluon emitted must also satisfy $E_5 > E_{cut}$.

First, all momenta are scaled by $\sqrt{\hat{s}} = \sqrt{2p_1 \cdot p_2}$. Working in the partonic centre-of-mass frame, the following variables can be defined as

$$p_i = \sqrt{\hat{s}} \; \hat{p}_i, \qquad y_{ij} = 2\hat{p}_i \cdot \hat{p}_j, \qquad \hat{m}^2 = m_t^2/\hat{s}, \qquad \beta = \sqrt{1 - 4\hat{m}}, \qquad w = \frac{E_{cut}}{\sqrt{\hat{s}}}. \tag{20}$$

The four-momentum vectors can be set up in the same manner as Equation 13 under the constraints

$$p_1^2 = p_2^2 = 0, \qquad p_3^2 = p_4^2 = m_t^2, \qquad p_5^2 = 0$$
$$\vec{p}_1 + \vec{p}_2 = 0, \qquad \vec{p}_3 + \vec{p}_4 + \vec{p}_5 = 0. \tag{21}$$

A suitable configuration is

$$\hat{p}_1 = \frac{1}{2}(1, sin\theta cos\phi, sin\theta sin\phi, cos\theta)$$

$$\hat{p}_2 = \frac{1}{2}(1, -sin\theta cos\phi, -sin\theta sin\phi, -cos\theta)$$

$$\hat{p}_3 = (E_3, 0, 0, k_3)$$

$$\hat{p}_4 = (1 - E_3 - E_5, -E_5 sin\alpha, 0, -k3 + E_5 cos\alpha)$$

$$\hat{p}_5 = E_5(1, sin\alpha, 0, -cos\alpha) \tag{22}$$

where α is the angle between the z-axis and the outgoing gluon. From this configuration, four-momentum conservation can be used to define invariants in terms of the phase-space integration variables to impose integration limits. Details of the calculation are provided in Appendix C. The limits of the integrations variables are

$$-1 \leq cos\theta \leq 1$$

$$0 \leq \phi \leq 2\pi$$

$$w(1 - \beta) \leq y_{45} \leq 1 - 2\hat{m}$$

$$\frac{E_3 - k_3}{1 - E_3 + k_3} y_{45} \leq y_{35} \leq \frac{E_3 + k_3}{1 - E_3 - k_3} y_{45}. \tag{23}$$

Now the hadronic charge asymmetries can be calculated by integrating over the appropriate phase space and convoluting with the PDFs. However, for the total asymmetric cross section, $\{q\bar{q}, \bar{q}q\}$ induced reactions in the quark-antiquark channel and $\{qg, \bar{q}g, gq, g\bar{q}\}$ induced reactions in the quark-gluon channel must be considered. Defining the function

$$F_{ij} = \int dx_1 dx_2 f_{i/N_1}(x_1, \mu_F) f_{j/N_2}(x_2, \mu_F), \tag{24}$$

and using equation (9), the total asymmetric cross section can be written as

$$\begin{aligned}
\sigma_A(S, m_t) = {} & F_{q\bar{q}} \; \hat{\sigma}_A^{q\bar{q}} + F_{\bar{q}q} \; \hat{\sigma}_A^{\bar{q}q} \quad \} \; q\bar{q} \; channel \\
& + F_{qg} \; \hat{\sigma}_A^{qg} + F_{\bar{q}g} \; \hat{\sigma}_A^{\bar{q}g} \\
& + F_{gq} \; \hat{\sigma}_A^{gq} + F_{g\bar{q}} \; \hat{\sigma}_A^{g\bar{q}}
\end{aligned} \Bigg\} \; qg \; channel \tag{25}$$

The $\hat{\sigma}_A^{q\bar{q}}$ and $\hat{\sigma}_A^{qg}$ are the only cross sections provided in the appendix. The other cross sections can be attained by explicitly renaming momenta or through charge conjuga-

tion.

$$\hat{\sigma}_A^{\bar{q}q} = \hat{\sigma}_A^{q\bar{q}} \ (p_1 \leftrightarrow p_2) = -\hat{\sigma}_A^{q\bar{q}} \tag{26}$$

$$\hat{\sigma}_A^{\bar{q}g} = -\hat{\sigma}_A^{qg} \tag{27}$$

$$\hat{\sigma}_A^{gq} = \hat{\sigma}_A^{qg}(p_1 \leftrightarrow p_2) = -\hat{\sigma}_A^{g\bar{q}} \tag{28}$$

Finally, the hadronic asymmetries can be given by

$$\begin{aligned}
\sigma_A(S, m_t) = &(F_{q\bar{q}} - F_{\bar{q}q}) \ \hat{\sigma}_A^{q\bar{q}} \\
&+ \big[(F_{qg} - F_{\bar{q}g}) \ \hat{\sigma}_A^{qg} \\
&+ (F_{gq} - F_{g\bar{q}}) \ \hat{\sigma}_A^{qg}(p_1 \leftrightarrow p_2) \big].
\end{aligned}$$

Before the values of the charge asymmetry are calculated, it is necessary to check that the phase-space slicing method is valid by showing that the quark-antiquark contribution to the cross section, $(F_{q\bar{q}} - F_{\bar{q}q})\sigma_A^{q\bar{q}}$, has no dependence on the energy cutoff for the soft gluon.

This independence of the soft and hard components is shown in Figure 5 using PDF set CTEQ6.6 for a $p\bar{p}$ collision at an energy of 1.96 TeV. The soft and hard contributions to the cross section, together with their sum, are plotted as a functions of the cutoff energy, E_{cut}. The soft and hard radiation contribute with opposing signs, with the former always larger than the latter. In the approximation that E_{cut} is small, the sum converges to the same result and therefore has no dependence on E_{cut}. Having made this check, the results can be binned into histograms and values for the charge asymmetry can be calculated.
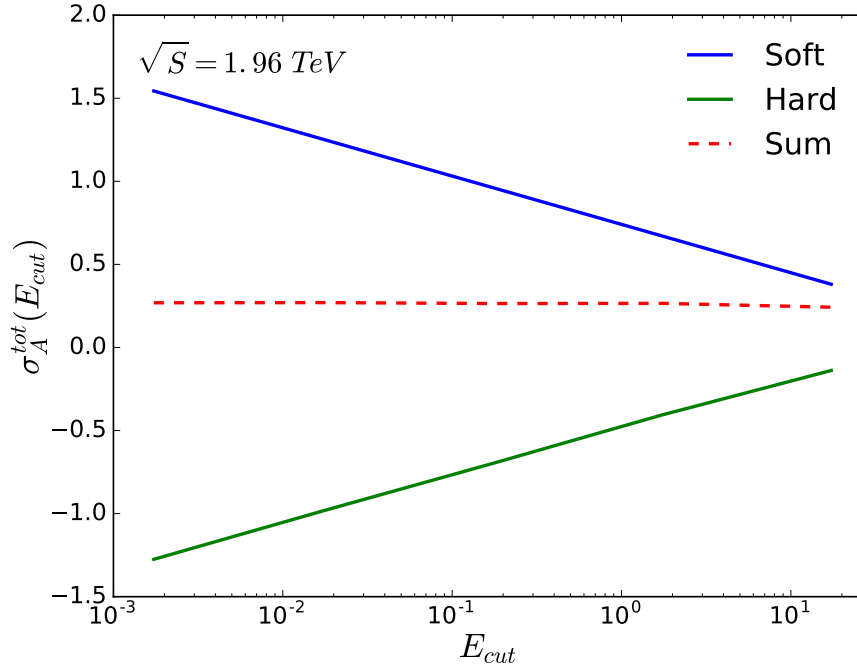
Figure 5: The NLO contribution to the asymmetric cross section for $q\bar{q}$ annihilation for a $p\bar{p}$ collision at an energy of $1.96\ TeV$. The PDF set CTEQ6.6 is used. The soft and hard contributions and their sum are shown as a function of the soft cutoff, E_{cut}. The resulting sum shows, in the approximation that E_{cut} is small, there is no dependence on E_{cut}.

4 Tevatron

In this section the charge asymmetry is investigated at the Tevatron, which is a proton-antiproton collider. As mentioned in Section 1.1, the charge asymmetry can be measured as a FB asymmetry due to charge conjugation invariance and is given by Equation 3. The asymmetry can be measured in both the lab and $t\bar{t}$ frame by performing a Lorentz transformation along the z-axis. The appropriate boost factor between the lab and centre-of-mass frames is given by [7],

$$\beta = \frac{x_2 - x_1}{x_2 + x_1}.\tag{29}$$

It is important to note that the asymmetry itself is calculated as a perturbative expansion in α_s. For the calculations carried out in this report, the numerator is evaluated at NLO to order α_s^3 and the denominator at LO to order α_s^2. Hence, the first non-vanishing contribution to the asymmetry is calculated which is referred to as NLO [10].

In the following section, the predictions for the FB asymmetry are provided along with comparisons to experimental data obtained by the CDF collaboration (using 5.3 fb^{-1} of

data) [20]. The MC predictions agree with the SM predictions and are binned to produce distributions that are comparable to [10]. However, there is a large discrepancy with the experimental data. In the analysis carried out here, NLO PDF sets are considered. In particular, the main focus will be on the MSTW2008 PDF set which has a 90% confidence level (CL) and with $\alpha_s(m_Z) = 0.118$. The PDF sets CTEQ6.6 and NNPDF23 will also be considered. For all results, a top quark mass of $m_t = 173.1 GeV$ is used and the factorisation and renormalisation scales are fixed to be $\mu_F = \mu_R = m_t$.

4.1   Results

4.1.1   Lab Rest Frame

The results for the asymmetric and symmetric cross sections and the total FB asymmetry in the lab frame are given in Table 1. The central value is obtained at a factorisation scale of $\mu_f = m_t$. The uncertainties arise from scale variations, which are estimated by setting μ_f to be $m_t/2$ and $2m_t$.

$PDFset$	$\sigma_A^{lab}[pb]$	$\sigma_S^{lab}[pb]$	$A_{FB}^{lab}(\%)$
$MSTW2008$	$0.257^{+0.137}_{-0.083}$	$5.398^{+2.190}_{-1.433}$	$4.76^{+0.44}_{-0.38}$
$CTEQ6.6$	$0.253^{+0.132}_{-0.080}$	$5.451^{+2.159}_{-1.423}$	$4.64^{+0.42}_{-0.36}$
$NNPDF2.3$	$0.258^{+0.136}_{-0.075}$	$5.420^{+2.130}_{-1.340}$	$4.76^{+0.46}_{-0.27}$
$CDF\,7\,TeV$			15.0 ± 5.5

Table 1: The asymmetric and symmetric cross sections and total FB asymmetry in the lab frame ($p\bar{p}$). The scale uncertainties arise from varying the factorisation scale, $\mu_f \in \{m_t/2, m_t \times 2\}$. CDF data [20] is also included as a comparison.

The results here disagree with the experimental data from the CDF. However, the cross sections and values for the FB asymmetry obtained with different PDF sets are well within their estimated uncertainties and also agree with the SM predictions in [21] and [10], obtained using MadGraph [9]. The work presented in this report may be validated further by reproducing the distributions in [10] for the asymmetric cross section and FB asymmetry. Figure 6 shows the differential asymmetric cross section (left plot) and FB asymmetry (right plot) as functions of the top quark rapidity, y_t. In both distributions, the scale uncertainties are shown by varying $\mu_f \in \{m_t/2, m_t \times 2\}$. The rapidity dependent

asymmetry is defined as [10]

$$A^{lab}_{FB}(y_t) = \frac{\left(\frac{d\sigma}{dy_t}\right)_F - \left(\frac{d\sigma}{dy_t}\right)_B}{\left(\frac{d\sigma}{dy_t}\right)_F + \left(\frac{d\sigma}{dy_t}\right)_B} = \frac{\frac{d\sigma^{lab}_A}{dy_t}}{\frac{d\sigma^{lab}_S}{dy_t}} , \tag{30}$$

where the ratio of the binned distributions for the asymmetric cross section and symmetric cross section is simply taken. This is repeated later for the invariant mass, $M_{t\bar{t}}$, and rapidity difference, $\Delta y = y_t - y_{\bar{t}}$, in the $t\bar{t}$ rest frame.
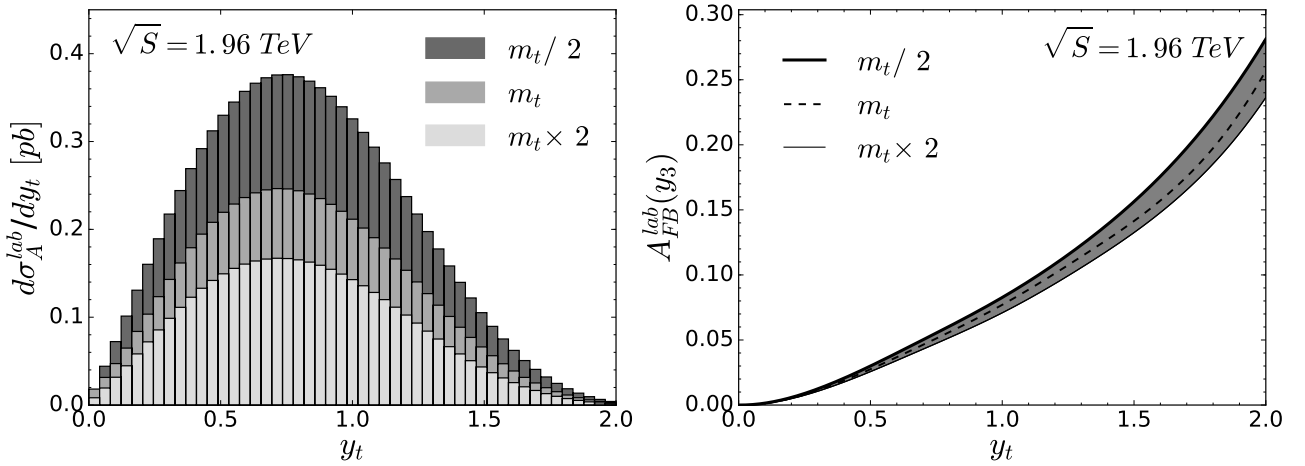

Figure 6: Left: The asymmetric differential cross section $d\sigma^{lab}_{FB}/dy_t$ as a function of the top quarks rapidity. Right: The FB asymmetry $A^{lab}_{FB}(y_t)$ as a function of the top quarks rapidity for PDF set MSTW2008. The distributions for $\mu_f \in \{m_t/2, m_t \times 2\}$ represent the scale uncertainties.

The right panel shows that the rapidity dependent asymmetry increases with respect to y_t. From the analysis carried out, the central region is found to be dominated by gluon fusion processes, which have the largest contribution to the symmetric cross section. However, as shown in Figure 7, this is increasingly suppressed at higher rapidities and becomes more comparable to asymmetric contribution, which leads to an increase in the asymmetry. Also note that the uncertainties for the FB asymmetry in the right panel are a lot smaller than the uncertainties produced for the differential asymmetric cross section shown in the left panel. This observation is due to propagation of the error when the ratio of the asymmetric cross section and symmetric cross section is taken. This uncertainty decrease also applies to the proceeding $t\bar{t}$ frame calculations.
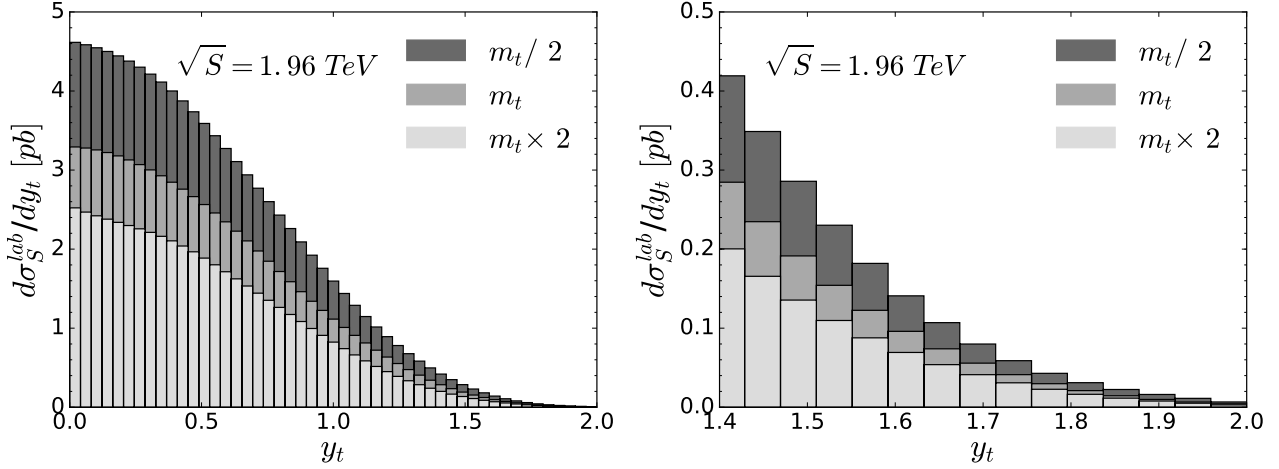
Figure 7: Left: The symmetric differential cross section $d\sigma_S^{lab}/dy_t$ in the forward hemisphere as a function of the top quarks rapidity. Right: An enhancement for the region $1.4 < y_t < 2.0$ using PDF set MSTW2008. The distributions for $\mu_f \in \{m_t/2, m_t \times 2\}$ represent the scale uncertainties.

4.1.2   Top Quark Pair Rest Frame

The results for the asymmetric and symmetric cross sections, and the total FB asymmetry in the $t\bar{t}$ frame are given in Table 2. Once again, the central value is given for a factorisation scale, $\mu_f = m_t$, while the uncertainties arise from scale variations, $\mu_f \in \{m_t/2, m_t \times 2\}$. From these results, it is observed that the three different PDF sets agree within their uncertainties and agree with the SM predictions in [10][21]. There is also an increase in the measured asymmetry compared to the lab frame. However the discrepancy with the experimental data from CDF is still observed.

PDFset	$\sigma_A^{tt}[pb]$	$\sigma_S^{tt}[pb]$	$A_{FB}^{tt}(\%)$
$MSTW2008$	$0.392_{-0.127}^{+0.209}$	$5.398_{-1.432}^{+2.189}$	$7.26_{-0.58}^{+0.66}$
$CTEQ6.6$	$0.386_{-0.123}^{+0.202}$	$5.450_{-1.423}^{+2.161}$	$7.08_{-0.56}^{+0.65}$
$NNPDF2.3$	$0.395_{-0.120}^{+0.206}$	$5.420_{-1.346}^{+2.126}$	$7.29_{-0.53}^{+0.26}$
$CDF\,7\,TeV$			15.8 ± 7.5

Table 2: The asymmetric and symmetric cross sections and total FB asymmetry in the $t\bar{t}$ frame. The uncertainties arise from varying the factorisation scale, $\mu_f \in \{m_t/2, m_t \times 2\}$. CDF data [20] is also included as a comparison.

In Figure 8 the differential asymmetric cross (left plot) and the FB asymmetry (right plot) are shown as functions of the invariant mass. Most of contribution to asymmetric cross section is found between the $380\ GeV < M_{t\bar{t}} < 500\ GeV$ bins. From the right plot, a dramatic increase in the asymmetry with respect to $M_{t\bar{t}}$ is shown, which reaches around 9% at $800GeV$. However, for $M_{t\bar{t}} > 800\ GeV$ the asymmetry becomes unstable. This instability is because the energy region is not only experimentally difficult to observe, but also difficult for the MC program to access due to the low probability of occurrence.

Events can be separated into high ($>\ M_{t\bar{t}}$) and low ($<\ M_{t\bar{t}}$) invariant mass bins in a similar manner to the CDF collaboration. These results are shown in Table 3, along with comparisons to CDF data [20]. From the data produced, there is a small increase in the FB asymmetry for the larger bin. However, it does not reduce the discrepancy between theory and experiment. The generated values differ from the SM predictions in [10]. The MC program used for this report predicts a larger (smaller) asymmetric and symmetric cross section in the $M_{t\bar{t}} < 450\ GeV$ ($M_{t\bar{t}} > 450\ GeV$) bin resulting in a larger (smaller) measured asymmetry.

Figure 8: Left: The asymmetric differential cross section $d\sigma_{FB}^{lab}/dM_{t\bar{t}}$ as a function of invariant mass. Right: The FB asymmetry $A_{FB}^{lab}(M_{t\bar{t}})$ for PDF set MSTW2008. The distributions for $\mu_f \in \{m_t/2, m_t \times 2\}$ represent the scale uncertainties.

The FB asymmetry can also be measured as a function of the rapidity difference, $\Delta y = y_t - y_{\bar{t}}$, in the $t\bar{t}$ rest frame, which is a particularly useful observable as it is Lorentz invariant. The results for the differential asymmetric cross section and FB asymmetry are shown as functions of Δy in Figure 9. The asymmetry is observed to increase with the respect to Δy, analogous to the relationship in Figure 6.

PDFset	$M_{t\bar{t}} < 450 GeV$			$M_{t\bar{t}} > 450 GeV$		
	$\sigma_A^{tt}[pb]$	$\sigma_S^{tt}[pb]$	$A_{FB}^{tt}(\%)$	$\sigma_A^{tt}[pb]$	$\sigma_S^{tt}[pb]$	$A_{FB}^{tt}(\%)$
$MSTW2008$	$0.228^{+0.117}_{-0.072}$	$3.365^{+1.305}_{-0.867}$	$6.79^{+0.61}_{-0.55}$	$0.163^{+0.092}_{-0.055}$	$2.033^{+0.884}_{-0.565}$	$8.04^{+0.71}_{-0.62}$
$CTEQ6.6$	$0.224^{+0.113}_{-0.069}$	$3.376^{+1.276}_{-0.855}$	$6.64^{+0.61}_{-0.50}$	$0.162^{+0.089}_{-0.054}$	$2.074^{+0.885}_{-0.568}$	$7.80^{+0.69}_{-0.64}$
$NNPDF2.3$	$0.230^{+0.115}_{-0.067}$	$3.372^{+1.265}_{-0.813}$	$6.81^{+0.61}_{-0.47}$	$0.166^{+0.091}_{-0.052}$	$2.048^{+0.861}_{-0.533}$	$8.08^{+0.75}_{-0.60}$
CDF			$-11.6^{+15.3}_{-15.3}$			$47.5^{+11.2}_{-11.2}$

Table 3: The asymmetric and symmetric cross sections and FB asymmetry compared in the low invariant mass ($< 450\ GeV$) and high invariant mass ($> 450\ GeV$) bins. The uncertainties arise from varying the factorisation scale, $\mu_f \in \{m_t/2, m_t \times 2\}$. CDF data [20] is also included as a comparison.
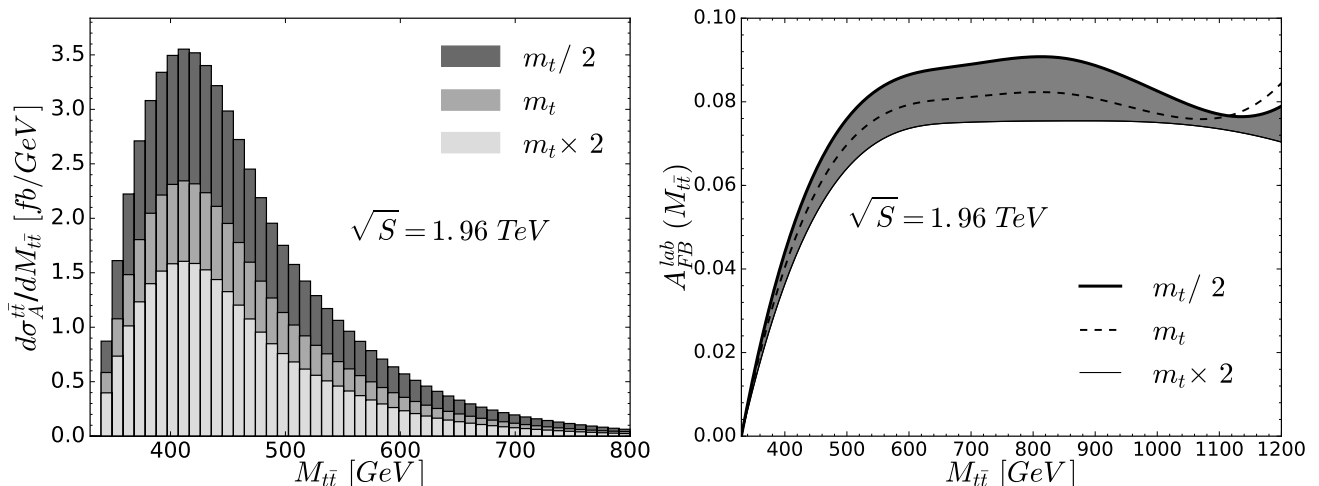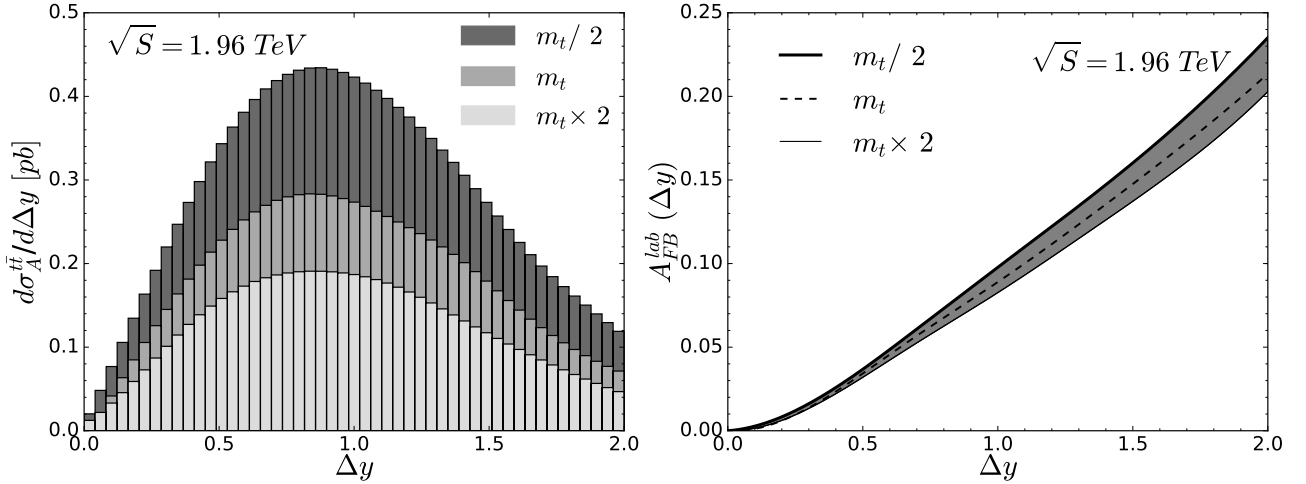

Figure 9: Left: The asymmetric differential cross section $d\sigma_{FB}^{lab}/d\Delta y$ as a function of invariant mass. Right: The FB asymmetry $A_{FB}^{lab}(\Delta y)$ for PDF set MSTW2008. The distributions for $\mu_f \in \{m_t/2, m_t \times 2\}$ represent the scale uncertainties.

The events can be separated into bins for $\Delta y < 1$ and $\Delta y > 1$, to make comparisons to CDF data, as shown in Table 4. For $\Delta y < 1$, the prediction is within the uncertainties of the CDF measurements [20], but not for $\Delta y > 1$. On the other hand, results generated here are consistent with the SM predictions reported in [10].

PDFset	$\Delta y < 1$			$\Delta y > 1$		
	$\sigma_A^{tt}[pb]$	$\sigma_S^{tt}[pb]$	$A_{FB}^{tt}(\%)$	$\sigma_A^{tt}[pb]$	$\sigma_S^{tt}[pb]$	$A_{FB}^{tt}(\%)$
MSTW2008	$0.201^{+0.103}_{-0.064}$	$4.203^{+1.674}_{-1.100}$	$4.78^{+0.40}_{-0.34}$	$0.191^{+0.105}_{-0.063}$	$1.195^{+0.515}_{-0.331}$	$15.98^{+1.36}_{-1.20}$
CTEQ6.6	$0.198^{+0.100}_{-0.062}$	$4.230^{+1.642}_{-1.089}$	$4.68^{+0.39}_{-0.35}$	$0.188^{+0.102}_{-0.061}$	$1.220^{+0.519}_{-0.334}$	$15.41^{+1.30}_{-1.10}$
NNPDF2.3	$0.202^{+0.102}_{-0.069}$	$4.224^{+1.628}_{-1.035}$	$4.78^{+0.41}_{-0.33}$	$0.193^{+0.104}_{-0.060}$	$1.196^{+0.499}_{-0.311}$	$16.14^{+1.40}_{-1.07}$
CDF			$2.6^{+11.8}_{-11.8}$			$61.1^{+25.6}_{-25.6}$

Table 4: The asymmetric and symmetric cross sections and FB asymmetry compared in bins, $\Delta y < 1$ and $\Delta y > 1$. The uncertainties arise from varying the factorisation scale, $\mu_f \in \{m_t/2, m_t \times 2\}$. CDF data [20] is also included as a comparison.

Overall, an MC program has been written which directly calculates the FB asymmetry at the Tevatron and agrees with SM predictions from [10][21]. However, there is a large discrepancy between the theoretical results and the experimental measurements from the CDF collaboration [20] at the Tevatron. This discrepancy may suggest that there are asymmetric production mechanisms that are beyond the SM. From the invariant mass and Δy distributions, the FB asymmetry was found to increase with respect to these observables. This increase in the asymmetry is because of the move from the central region which is dominated by gluon-fusion. It is desirable to adapt the MC program used here to be more appropriate for the LHC which can achieve higher rapidities and invariant masses due to its larger colliding energy.

5   LHC

In this section the predictions for the charge asymmetry at the LHC are discussed. This includes the necessary adaptations to the MC program for studying the charge asymmetry. First, note that the LHC is a proton-proton collider and therefore, one can no longer measure the asymmetry as a FB asymmetry due to its symmetric initial state [5]. While the production rates for the top and antitop quarks in the forward and backward hemispheres are the same, it is still possible to investigate the charge asymmetry by restricting ourselves to kinematic regions where gluon fusion processes are suppressed and quark-antiquark annihilation processes are enhanced. This investigation is achieved by introducing cut-independent and cut-dependent asymmetries. Due to the large contribution from gluon fusion processes, the charge asymmetry measured at the LHC is smaller than

at the Tevatron. Nevertheless, through the cut-dependent definitions used, it is possible to show, at the LHC, that the top quarks are more abundantly produced at higher rapidities while antitops are more centrally produced as discussed in [10], [16], [22], [23].

For the following analysis, the PDF set MSTW2008 at NLO with a CL 90 and $\alpha_s(m_Z) = 0.118$ is used. Comparisons are made with experimental measurements carried out at the CMS [24] and ATLAS [25][26] detectors as well as SM predictions from [15] and [23] to test the validity of the MC program. Note that the analysis in [23] includes electroweak corrections which amount to a factor of roughly 1.1 in the asymmetry.

5.1   Results

5.1.1   Cut-Independent Asymmetries

The following cut-independent asymmetries are considered, which depend on the rapidity and pseudorapidity of the top and antitop quarks. A similar analysis was carried out for the LHC by the CMS [24] and ATLAS [25][26] detectors. The pseudorapidity is the rapidity in the approximation that the mass of the particle is negligible as so the $p \to E$ [7]. It is therefore given by

$$\eta = \frac{1}{2} \ln \left(\frac{|p| + p_z}{|p| - p_z} \right) = -\ln \left[tan \left(\frac{\theta}{2} \right) \right]. \tag{31}$$

The cut independent asymmetries are given by

$$A_C^y = \frac{N(\Delta_y > 0) - N(\Delta_y < 0)}{N(\Delta_y > 0) + N(\Delta_y < 0)} = \frac{\sigma(\Delta_y > 0) - \sigma(\Delta_y < 0)}{\sigma(\Delta_y > 0) + \sigma(\Delta_y < 0)} = \frac{\sigma_A^y}{\sigma_S^y} \tag{32}$$

and

$$A_C^\eta = \frac{N(\Delta_\eta > 0) - N(\Delta_\eta < 0)}{N(\Delta_\eta > 0) + N(\Delta_\eta < 0)} = \frac{\sigma(\Delta_\eta > 0) - \sigma(\Delta_\eta < 0)}{\sigma(\Delta_\eta > 0) + \sigma(\Delta_\eta < 0)} = \frac{\sigma_A^\eta}{\sigma_S^\eta} \tag{33}$$

where $\Delta_y = |y_t| - |y_{\bar{t}}|$ and $\Delta_\eta = |\eta_t| - |\eta_{\bar{t}}|$ are calculated in the lab frame. Once again, the asymmetry is calculated by considering the asymmetric and symmetric terms which are given at NLO and LO respectively.

The asymmetric and symmetric cross sections and cut-independent charge asymmetries are given in Table 5 and Table 6, at different LHC energies. The predictions produced from the MC program for A_C^y and A_C^η are within the uncertainties of the experimental results from the LHC. However, the experimental uncertainties are dominant in both the CMS [24] and ATLAS [25][26] measurements. Hence, better measurements are required to improve the analysis carried out. Also, the results are comparable to the SM predictions

in [23] if a factor of 1.1 for the weak and QED corrections are included. For both cut-independent asymmetries a decrease in the measured asymmetry is observed, when moving to higher LHC energies. This is due to a larger contribution to the symmetric cross section from gluon fusion processes. Hence, cut-dependent asymmetries are defined such that kinematic regions can be explicitly chosen where gluon fusion is suppressed and quark-antiquark annihilation is enhanced.

	σ_A^y	σ_S^y	$A_C^y(\%)$
7 TeV	$1.084^{+0.458}_{-0.244}$	$107.248^{+24.227}_{-18.041}$	$1.01^{+0.16}_{-0.07}$
8 TeV	$1.370^{+0.501}_{-0.321}$	$152.829^{+34.509}_{-25.678}$	$0.90^{+0.10}_{-0.07}$
10 TeV	$1.994^{+0.675}_{-0.471}$	$268.169^{+60.623}_{-45.151}$	$0.74^{+0.07}_{-0.06}$
12 TeV	$2.630^{+1.035}_{-0.675}$	$414.167^{+93.439}_{-69.834}$	$0.64^{+0.09}_{-0.07}$
14 TeV	$3.245^{+1.066}_{-0.725}$	$588.679^{+132.895}_{-98.883}$	$0.55^{+0.05}_{-0.04}$
ATLAS 7 TeV			$-1.9 \pm 2.8 \pm 2.4$
ATLAS 8 TeV			0.9 ± 0.5

Table 5: The asymmetric and symmetric cross sections and cut-independent charge asymmetry calculated with Δy in the lab frame (pp) for a range of LHC energies. The uncertainties arise from varying the factorisation scale, $\mu_f \in \{m_t/2, m_t \times 2\}$. Data from ATLAS is provided for 7 TeV [25] and 8 TeV [26].

	σ_A^{lab}	σ_S^{lab}	$A_C^{\eta}(\%)$
7 TeV	$1.177^{+0.429}_{-0.287}$	$107.251^{+24.252}_{-18.033}$	$1.10^{+0.12}_{-0.10}$
8 TeV	$1.490^{+0.510}_{-0.364}$	$152.825^{+34.485}_{-25.694}$	$0.97^{+0.09}_{-0.09}$
10 TeV	$2.132^{+0.769}_{-0.522}$	$268.178^{+60.726}_{-45.108}$	$0.80^{+0.09}_{-0.07}$
12 TeV	$2.779^{+0.989}_{-0.701}$	$414.234^{+93.518}_{-69.905}$	$0.67^{+0.07}_{-0.07}$
14 TeV	$3.445^{+1.167}_{-0.816}$	$588.655^{+133.228}_{-99.059}$	$0.59^{+0.05}_{-0.05}$
CMS 7 TeV			$-1.6 \pm 3.0^{+1.0}_{-1.9}$

Table 6: The asymmetric and symmetric cross sections and cut-independent charge asymmetry calculated with $\Delta\eta$, in the lab frame (pp) for a range of LHC energies. The uncertainties arise from varying the factorisation scale, $\mu_f \in \{m_t/2, m_t \times 2\}$. CMS data [24] at 7 TeV is also provided as a comparison.

5.1.2 Cut-Dependent Asymmetries

As shown in [23], asymmetries that depend on a cut, y_{cut}, are defined and demonstrate that top quarks are preferentially produced at larger rapidities while antitops are produced more centrally. The definitions are given by

$$A_C^{in}(y_{cut}) = \frac{N(|y_{\bar{t}}| \leq y_{cut}) - N(|y_t| \leq y_{cut})}{N(|y_{\bar{t}}| \leq y_{cut}) + N(|y_t| \leq y_{cut})} = \frac{\sigma(|y_{\bar{t}}| \leq y_{cut}) - \sigma(|y_t| \leq y_{cut})}{\sigma(|y_{\bar{t}}| \leq y_{cut}) + \sigma(|y_t| \leq y_{cut})}, \quad (34)$$

and

$$A_C^{out}(y_{cut}) = \frac{N(|y_t| > y_{cut}) - N(|y_{\bar{t}}| > y_{cut})}{N(|y_t| > y_{cut}) + N(|y_{\bar{t}}| > y_{cut})} = \frac{\sigma(|y_t| > y_{cut}) - \sigma((|y_{\bar{t}}| > y_{cut})}{\sigma(|y_t| > y_{cut}) + \sigma(|y_{\bar{t}}| > y_{cut})}, \quad (35)$$

where the asymmetries are measured in the lab frame. Note that Equation 34 is constructed to give a positive asymmetry by considering the top and antitops in the backward hemisphere.

In Figure 10, Equation 35 is used to show the total asymmetric cross section and the total symmetric contributions from gluon fusion and quark-antiquark annihilation as fuctions of y_{cut} on the left and right, respectively. The scale variations are plotted in the same procedure as section 4.1. The dependence on y_{cut} is shown in Figure 11 for A_C^{in} and

A_C^{out}. This is carried out for the LHC operating at $7\ TeV$ on the left plot and $14\ TeV$ on the right plot. A further restriction is also included on the rapidity of the top and antitop quarks where $|y_t|, |y_{\bar{t}}| < 2.5$. Additional tables for the asymmetric and symmetric cross section and charge asymmetry are provided in Appendix A for the cut-dependent asymmetries at $7\ TeV$ and $14\ TeV$.
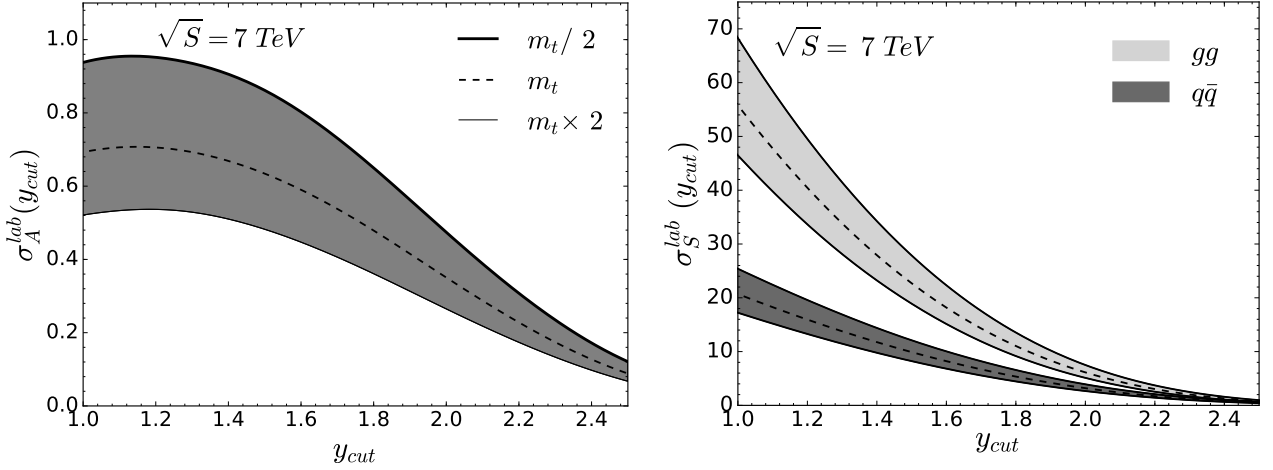
Figure 10: Left: The total asymmetric cross section $\sigma_A^{lab}(y_{cut})$ from A_C^{out} as a function of y_{cut}. Right: The LO symmetric contributions $(gg, q\bar{q})$ from A_C^{out} as a function of the y_{cut}.
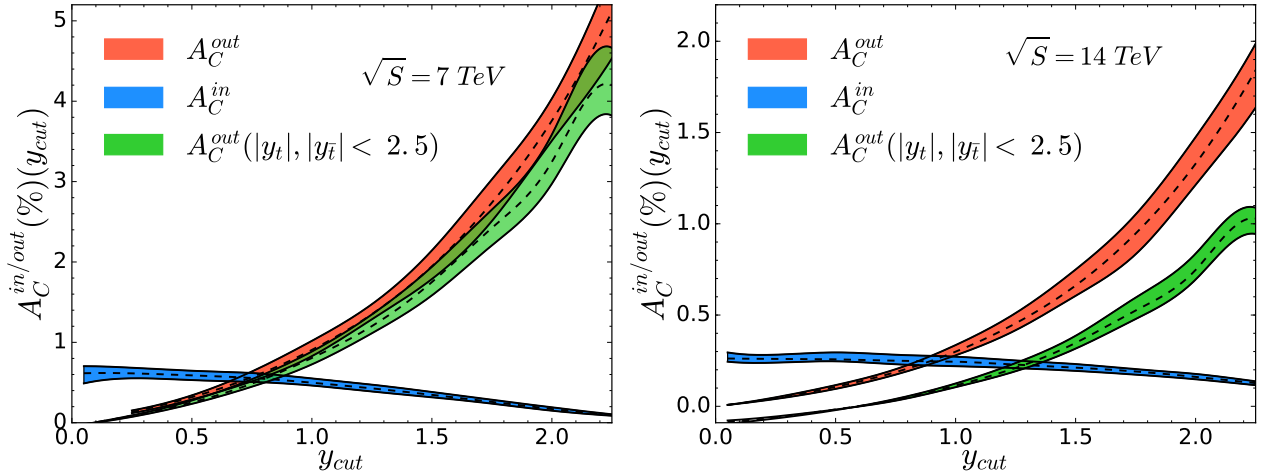

Figure 11: Left: The A_C^{in} and A_C^{out} as a function y_{cut} at LHC $7\ TeV$. Right: for LHC $14\ TeV$. An additional restriction on the top and antitop rapidity $|y_t|, |y_{\bar{t}}| < 2.5$ is shown in both plots.

For both plots in Figure 11, it is observed that $A_C^{in}(y_{cut}) > A_C^{out}(y_{cut})$ in the central region for $y_{cut} < 0.7$ while $A_C^{in}(y_{cut}) < A_C^{out}(y_{cut})$ for $y_{cut} > 0.7$ approximately. This observation is due to a decrease in top quarks in the central region and their enhancement at larger rapidities, which agrees with the observation in [23]. It is also observed that A_C^{out} is able to achieve larger asymmetries as the gluon fusion processes are more suppressed and become more comparable to the asymmetric cross section, illustrated in Figure 10. Furthermore, the additional restriction on the top and antitop rapidity ($|y_t|, |y_{\bar{t}}| < 2.5$) is more evidence that top quarks are preferentially produced at higher rapidities. The evidence comes from the restricted curve being $< A_C^{out}$. Additionally, the difference is more pronounced for the LHC operating at $14\ TeV$, which is due to higher rapidities being more accessible at larger colliding energies. However, it is important to note that these regions of high rapidities have low event rates and are difficult to experimentally observe.

6 Summary and Conclusions

In summary, an efficient method of calculating the charge asymmetry is provided using MC techniques. The differential cross sections contributing to the asymmetry are driven by quark-antiquark annihilation and quark-gluon scattering at NLO QCD (α_s^3), which is integrated using phase-space slicing, while the symmetric contribution is calculated at LO for gluon fusion and quark-antiquark processes. The resulting asymmetry is calculated at first non-vanishing order (α_s), referred to as NLO. While the charge asymmetry has previously been calculated to NNLO QCD (α_s^3) + NLO electro-weak ($\alpha\alpha_s^2$) [17], work reported here may be used as a template for higher-order corrections from soft-gluon resummation [10][15]. The method presented may also be used to calculate the charge asymmetry in $b\bar{b}$ production.

The forward-backward asymmetry was calculated for a $p\bar{p}$ collider, such as the Tevatron, which is analogous to the charge asymmetry due to charge conjugation invariance. Predictions for the total FB asymmetry and kinematic distributions were produced which agreed with [10] and [21]. However, there is still a large discrepancy when compared with data from the CDF collaboration [20].

The effects of the charge asymmetry were also studied for a pp collider, such as the LHC. Since the initial state is symmetric, the FB asymmetry is no longer applicable. Hence, predictions for cut-independent asymmetries were calculated, which are comparable to values predicted in [23]. Comparisons with existing measurements from ATLAS at $7\ TeV$ [25] and $8\ TeV$ [26] and also with CMS [24] at $7\ TeV$ were made. The SM predictions reported here agreed with the experimental measurements within their uncertainties. Although, experimental measurements with higher precision would clarify if these SM predictions are correct. Next, the MC program used was validated further by producing cut-dependent

plots, which agreed with the results in [23]. These plots show that top quarks are predominately produced at higher rapidities while antitops are produced more centrally. Overall, a reliable Monte Carlo program has been created for calculating the charge asymmetry which can serve as a template for the addition of higher order corrections.

References

[1] Kobayashi, M., Maskawa, T. (1973). *"CP-violation in the renormalizable theory of weak interaction"*. Progress of Theoretical Physics. https://doi.org/10.1143/PTP.49.652

[2] The CDF Collaboration. (1995)*"Observation of Top Quark Production in Pbar-P Collisions"*. https://doi.org/10.1103/PhysRevLett.74.2626

[3] Abachi, S. (1995). *"Observation of the Top Quark"*, 1–12. https://doi.org/10.1103/PhysRevLett.74.2632

[4] Kröninger, K., Meyer, A. B., Uwer, P. (2015). *"Top-Quark Physics at the LHC"*. https://doi.org/10.1007/978-3-319-15001-7_7

[5] Bernreuther, W. (n.d.). *"Top quark physics at the LHC"* arXiv : 0805 . 1333v1 [hep-ph] 9 May 2008.

[6] Papaefstathiou, A. (2014). *"How-to: Write a parton-level Monte Carlo event generator"*, (July), 20. Retrieved from http://arxiv.org/abs/1412.4677

[7] Han, T. (n.d.). *"COLLIDER PHENOMENOLOGY Basic Knowledge and Techniques"*, 1–51.

[8] Kühn, J., Rodrigo, G. (1998). *"Charge Asymmetry in Hadroproduction of Heavy Quarks"*. Physical Review Letters, 81(1), 49–52. https://doi.org/10.1103/PhysRevLett.81.49

[9] Alwall, J., Frederix, R., Frixione, S., Hirschi, V., Maltoni, F., Mattelaer, O., . . . Zaro, M. (2014)*"The automated computation of tree-level and next-to-leading order differential cross sections, and their matching to parton shower simulations"*. Journal of High Energy Physics, 2014(7). https://doi.org/10.1007/JHEP07(2014)079

[10] Ahrens, V., Ferroglia, A., Neubert, M., Pecjak, B. D., Yang, L. L. (2011). *"Top-pair forward-backward asymmetry beyond next-to-leading order"*. Physical Review D - Particles, Fields, Gravitation and Cosmology, 84(7), 1–12. https://doi.org/10.1103/PhysRevD.84.074004

[11] Peter Lepage, G. (1978)."*A new algorithm for adaptive multidimensional integration*". Journal of Computational Physics, 27(2), 192–203. https://doi.org/10.1016/0021-9991(78)90004-9

[12] Plehn, T. (2008). "*LHC Phenomenology for Physics Hunters*". https://doi.org/10.1142/9789812838360_0003

[13] Nazionale, I., Milano, S. (2006)."*On the running coupling constant in QCD*" arXiv : hep-ph / 0607209v2 12 Oct 2006, 1–75.

[14] Duca, V. Del, Elektronen-synchrotron, D. (1995). "*An introduction to the perturbative QCD pomeron and to jet physics at large rapidities 1 Introduction*", (February).

[15] Kidonakis, N., Pecjak, B. D. (2012). "*Top-quark production and QCD*". European Physical Journal C, 72(7), 1–19. https://doi.org/10.1140/epjc/s10052-012-2084-0

[16] Kühn, J. H., Rodrigo, G. (1998). "*Charge asymmetry of heavy quarks at hadron colliders*". Physical Review D, 59(5), 1–16.

[17] Czakon, M., Heymes, D., Mitov, A., Pagani, D., Tsinikos, I., Zaro, M. (2017). *The top-quark charge asymmetry at the LHC and Tevatron through NNLO QCD and NLO EW*. https://doi.org/10.1007/JHEP10(2017)186

[18] Schwartz, M. D. (2013). "*Quantum field theory and the Standard Model*".

[19] Harris, B. W., Owens, J. F. (2002). "*Two cutoff phase space slicing method*". Physical Review D - Particles, Fields, Gravitation and Cosmology, 65(9B)

[20] T. Aaltonen et al. [CDF Collaboration], Phys. Rev. D83, 112003 (2011). [arXiv:1101.0034 [hep-ex]].

[21] Bernreuther, W., Si, Z. G. (2012). "*Top quark and leptonic charge asymmetries for the Tevatron and LHC*". Physical Review D - Particles, Fields, Gravitation and Cosmology, 86(3). https://doi.org/10.1103/PhysRevD.86.034026

[22] Antuñano, O., Kühn, J. H., Rodrigo, G. (2008). "*Top quarks, axigluons, and charge asymmetries at hadron colliders*. Physical Review D - Particles, Fields, Gravitation and Cosmology, 77(1). https://doi.org/10.1103/PhysRevD.77.014003

[23] Kühn, J. H., Rodrigo, G. (2012). "*Charge asymmetries of top quarks at hadron colliders revisited*". Journal of High Energy Physics, 2012(1). https://doi.org/10.1007/JHEP01(2012)063

[24] [CMS Collaboration], CMS-PAS-TOP-10-010, CMS-PAS-TOP-11-014.

[25] ATLAS Collaboration. (2012). "*Measurement of the charge asymmetry in top quark pair production in pp collisions at $\sqrt{s} = 7\ TeV$ using the ATLAS detector*". The European Physical Journal C, 72(6), 16–16. https://doi.org/10.1140/epjc/s10052-012-2039-5

[26] ATLAS Collaboration. (2016). "*Measurement of the charge asymmetry in top-quark pair production in the lepton-plus-jets final state in pp collision data at $\sqrt{s} = 8\ TeV$ with the ATLAS detector*". Eur. Phys. J. C, 76(August), 87. https://doi.org/10.1140/epjc/s10052-016-3910-6

Appendices

A   Data

In this section of the appendix we provide additional tables for plotted results in Figure 11 for the A_C^{in}, A_C^{out} along with calculated values for the asymmetric and symmetric cross sections at $7\,TeV$ and $14\,TeV$. We also include a table for A_C^{out} with the further restriction on the top and antitop rapidity ($|y_t|, |y_{\bar{t}}| < 2.5$)

y_C^{in}	$\sigma_A^{lab}[pb]$	$\sigma_S^{lab}[pb]$	$A_C^{in}(\%)$
0.05	$0.047^{+0.019}_{-0.016}$	$7.702^{+1.744}_{-1.251}$	$0.62^{+0.09}_{-0.13}$
0.25	$0.235^{+0.086}_{-0.059}$	$38.186^{+8.648}_{-6.425}$	$0.61^{+0.07}_{-0.06}$
0.50	$0.441^{+0.152}_{-0.111}$	$74.841^{+16.866}_{-12.642}$	$0.59^{+0.06}_{-0.06}$
0.75	$0.604^{+0.219}_{-0.145}$	$108.478^{+24.494}_{-18.261}$	$0.56^{+0.06}_{-0.05}$
1.00	$0.688^{+0.246}_{-0.156}$	$138.014^{+31.283}_{-23.169}$	$0.50^{+0.05}_{-0.04}$
1.25	$0.695^{+0.250}_{-0.171}$	$162.604^{+36.812}_{-27.371}$	$0.43^{+0.05}_{-0.04}$
1.50	$0.632^{+0.222}_{-0.151}$	$181.872^{+41.079}_{-30.493}$	$0.35^{+0.04}_{-0.03}$
1.75	$0.508^{+0.176}_{-0.121}$	$195.917^{+44.164}_{-32.957}$	$0.26^{+0.03}_{-0.02}$
2.00	$0.350^{+0.132}_{-0.095}$	$205.184^{+46.371}_{-34.580}$	$0.17^{+0.02}_{-0.02}$
2.25	$0.201^{+0.069}_{-0.049}$	$210.585^{+47.477}_{-35.456}$	$0.10^{+0.01}_{-0.01}$
2.50	$0.090^{+0.032}_{-0.022}$	$213.214^{+48.252}_{-35.841}$	$0.04^{+0.00}_{-0.00}$

Table A.1: The asymmetric and symmetric cross sections and A_C^{in} asymmetry for a range of y_{cut} at an LHC colliding energy of $7\,TeV$.

y_C^{in}	$\sigma_A^{lab}[pb]$	$\sigma_S^{lab}[pb]$	$A_C^{in}(\%)$
0.05	$0.092^{+0.034}_{-0.020}$	$35.188^{+7.645}_{-5.847}$	$0.26^{+0.03}_{-0.02}$
0.25	$0.455^{+0.151}_{-0.107}$	$174.823^{+39.640}_{-29.286}$	$0.26^{+0.02}_{-0.02}$
0.50	$0.887^{+0.359}_{-0.181}$	$344.688^{+77.444}_{-58.247}$	$0.26^{+0.04}_{-0.01}$
0.75	$1.260^{+0.485}_{-0.294}$	$504.591^{+113.607}_{-85.040}$	$0.25^{+0.03}_{-0.02}$
1.00	$1.592^{+0.576}_{-0.402}$	$650.595^{+146.651}_{-109.289}$	$0.24^{+0.03}_{-0.02}$
1.25	$1.781^{+0.618}_{-0.424}$	$779.834^{+176.038}_{-131.103}$	$0.23^{+0.02}_{-0.02}$
1.50	$1.886^{+0.640}_{-0.449}$	$889.680^{+201.291}_{-149.264}$	$0.21^{+0.02}_{-0.02}$
1.75	$1.869^{+0.572}_{-0.457}$	$979.519^{+221.654}_{-165.264}$	$0.19^{+0.01}_{-0.02}$
2.00	$1.693^{+0.591}_{-0.400}$	$1049.480^{+236.969}_{-177.187}$	$0.16^{+0.02}_{-0.01}$
2.25	$1.400^{+0.444}_{-0.345}$	$1100.967^{+249.717}_{-185.284}$	$0.13^{+0.01}_{-0.01}$
2.50	$1.043^{+0.347}_{-0.230}$	$1136.081^{+257.078}_{-190.855}$	$0.09^{+0.01}_{-0.01}$

Table A.2: The asymmetric and symmetric cross sections and A_C^{in} asymmetry for a range of y_{cut} at an LHC colliding energy of 14 TeV.

y_C^{out}	$\sigma_A^{lab}[pb]$	$\sigma_S^{lab}[pb]$	$A_C^{out}(\%)$
0.05	$0.048^{+0.017}_{-0.013}$	$206.816^{+46.722}_{-34.786}$	$0.02^{+0.00}_{-0.00}$
0.25	$0.233^{+0.081}_{-0.056}$	$176.304^{+39.850}_{-29.614}$	$0.13^{+0.01}_{-0.01}$
0.50	$0.444^{+0.151}_{-0.107}$	$139.651^{+31.609}_{-23.490}$	$0.32^{+0.03}_{-0.03}$
0.75	$0.601^{+0.211}_{-0.144}$	$105.994^{+23.974}_{-17.823}$	$0.57^{+0.06}_{-0.05}$
1.00	$0.693^{+0.245}_{-0.172}$	$76.484^{+17.273}_{-12.862}$	$0.91^{+0.09}_{-0.09}$
1.25	$0.701^{+0.244}_{-0.166}$	$51.893^{+11.749}_{-8.729}$	$1.35^{+0.13}_{-0.11}$
1.50	$0.634^{+0.227}_{-0.152}$	$32.606^{+7.364}_{-5.472}$	$1.95^{+0.21}_{-0.17}$
1.75	$0.509^{+0.182}_{-0.125}$	$18.599^{+4.187}_{-3.132}$	$2.74^{+0.30}_{-0.26}$
2.00	$0.350^{+0.124}_{-0.086}$	$9.327^{+2.112}_{-1.575}$	$3.76^{+0.39}_{-0.34}$
2.25	$0.200^{+0.070}_{-0.047}$	$3.914^{+0.896}_{-0.650}$	$5.12^{+0.50}_{-0.43}$
2.50	$0.088^{+0.032}_{-0.021}$	$1.287^{+0.290}_{-0.217}$	$6.87^{+0.80}_{-0.58}$

Table A.3: The asymmetric and symmetric cross sections and A_C^{out} asymmetry for a range of y_{cut} at an LHC colliding energy of $7\ TeV$.

y_C^{out}	$\sigma_A^{lab}[pb]$	$\sigma_S^{lab}[pb]$	$A_C^{out}(\%)$
0.05	$0.092^{+0.016}_{-0.023}$	$1142.197^{+256.973}_{-191.709}$	$0.01^{+-0.00}_{-0.00}$
0.25	$0.449^{+0.155}_{-0.114}$	$1002.467^{+225.503}_{-168.684}$	$0.04^{+0.00}_{-0.00}$
0.50	$0.887^{+0.297}_{-0.227}$	$832.859^{+187.721}_{-139.882}$	$0.11^{+0.01}_{-0.01}$
0.75	$1.259^{+0.418}_{-0.287}$	$672.804^{+152.442}_{-112.966}$	$0.19^{+0.02}_{-0.01}$
1.00	$1.576^{+0.584}_{-0.353}$	$526.333^{+117.550}_{-88.138}$	$0.30^{+0.04}_{-0.02}$
1.25	$1.808^{+0.682}_{-0.432}$	$397.780^{+89.616}_{-67.579}$	$0.45^{+0.06}_{-0.04}$
1.50	$1.903^{+0.737}_{-0.454}$	$287.568^{+64.708}_{-48.313}$	$0.66^{+0.09}_{-0.06}$
1.75	$1.873^{+0.672}_{-0.500}$	$197.928^{+44.209}_{-33.122}$	$0.95^{+0.10}_{-0.11}$
2.00	$1.698^{+0.615}_{-0.402}$	$127.757^{+29.035}_{-20.909}$	$1.33^{+0.15}_{-0.12}$
2.25	$1.407^{+0.451}_{-0.366}$	$76.398^{+17.139}_{-12.770}$	$1.84^{+0.15}_{-0.21}$
2.50	$1.022^{+0.361}_{-0.236}$	$41.205^{+9.297}_{-6.927}$	$2.48^{+0.26}_{-0.19}$

Table A.4: The asymmetric and symmetric cross sections and A_C^{out} asymmetry for a range of y_{cut} at an LHC colliding energy of $14\ TeV$.

y_C^{out}	$\sigma_A^{lab}[pb]$	$\sigma_S^{lab}[pb]$	$A_C^{out}(\%)$
0.05	$-0.041^{+-0.013}_{0.008}$	$205.515^{+46.447}_{-34.560}$	$-0.02^{+-0.00}_{0.00}$
0.25	$0.152^{+0.044}_{-0.046}$	$175.059^{+39.544}_{-29.470}$	$0.09^{+0.00}_{-0.01}$
0.50	$0.350^{+0.120}_{-0.080}$	$138.386^{+31.258}_{-23.273}$	$0.25^{+0.02}_{-0.02}$
0.75	$0.509^{+0.186}_{-0.119}$	$104.710^{+23.716}_{-17.643}$	$0.49^{+0.06}_{-0.04}$
1.00	$0.606^{+0.211}_{-0.152}$	$75.195^{+16.995}_{-12.636}$	$0.81^{+0.08}_{-0.08}$
1.25	$0.608^{+0.227}_{-0.140}$	$50.617^{+11.419}_{-8.528}$	$1.20^{+0.15}_{-0.09}$
1.50	$0.548^{+0.197}_{-0.135}$	$31.332^{+7.088}_{-5.260}$	$1.75^{+0.19}_{-0.17}$
1.75	$0.419^{+0.144}_{-0.102}$	$17.304^{+3.925}_{-2.900}$	$2.42^{+0.23}_{-0.22}$
2.00	$0.261^{+0.093}_{-0.062}$	$8.028^{+1.824}_{-1.347}$	$3.25^{+0.34}_{-0.27}$
2.25	$0.111^{+0.040}_{-0.027}$	$2.634^{+0.598}_{-0.441}$	$4.20^{+0.46}_{-0.38}$
2.50	$0.000^{+0.000}_{0.000}$	$0.000^{+0.000}_{0.000}$	$0.00^{+0.00}_{0.00}$

Table A.5: The asymmetric and symmetric cross sections and A_C^{out} asymmetry for a range of y_{cut} at an LHC colliding energy of $7\ TeV$. A futher restriction is imposed on the top and antitop rapidity, $(|y_t|, |y_{\bar{t}}| < 2.5)$.

y_C^{out}	$\sigma_A^{lab}[pb]$	$\sigma_S^{lab}[pb]$	$A_C^{out}(\%)$
0.05	$-0.940_{0.228}^{+-0.350}$	$1101.257_{-185.381}^{+248.619}$	$-0.09_{0.01}^{+-0.01}$
0.25	$-0.586_{0.139}^{+-0.199}$	$961.266_{-161.503}^{+217.325}$	$-0.06_{0.01}^{+-0.01}$
0.50	$-0.138_{0.021}^{+-0.066}$	$791.551_{-133.114}^{+179.019}$	$-0.02_{-0.00}^{+-0.00}$
0.75	$0.225_{-0.063}^{+0.088}$	$631.649_{-106.311}^{+142.562}$	$0.04_{-0.00}^{+0.00}$
1.00	$0.552_{-0.129}^{+0.192}$	$485.461_{-81.811}^{+109.751}$	$0.11_{-0.01}^{+0.01}$
1.25	$0.749_{-0.180}^{+0.286}$	$356.340_{-59.924}^{+80.450}$	$0.21_{-0.02}^{+0.03}$
1.50	$0.856_{-0.208}^{+0.311}$	$246.447_{-41.364}^{+55.527}$	$0.35_{-0.03}^{+0.04}$
1.75	$0.822_{-0.199}^{+0.323}$	$156.529_{-26.224}^{+35.671}$	$0.53_{-0.05}^{+0.07}$
2.00	$0.647_{-0.147}^{+0.240}$	$86.592_{-14.490}^{+19.487}$	$0.75_{-0.05}^{+0.09}$
2.25	$0.361_{-0.086}^{+0.107}$	$35.096_{-5.903}^{+7.980}$	$1.03_{-0.08}^{+0.06}$
2.50	$0.000_{0.000}^{+0.000}$	$0.000_{0.000}^{+0.000}$	$0.00_{0.00}^{+0.00}$

Table A.6: The asymmetric and symmetric cross sections and A_C^{out} asymmetry for a range of y_{cut} at an LHC colliding energy of $14\ TeV$. A futher restriction is imposed on the top and antitop rapidity, $(|y_t|, |y_{\bar{t}}| < 2.5)$.

B   Equations

We provide the differential cross sections necessary for calculating the charge asymmetry. These have been provided by [16] but are displayed here for the convenience of the reader. For the leading order symmetric cross section we have the processes for $q\bar{q}$ and gg fusion.

$$\frac{d\sigma_S^{q\bar{q}\to t\bar{t}}}{dcos\theta} = \alpha_s^2 \frac{T_F C_F}{N_C} \frac{\pi\beta}{2\hat{s}}(1 + c^2 + 4\hat{m}^2), \tag{B.1}$$

$$\frac{d\sigma_S^{gg\to t\bar{t}}}{dcos\hat{\theta}} = \alpha_s^2 \frac{\pi\beta}{2\hat{s}}\left(\frac{1}{N_C(1-c^2)} - \frac{T_F}{2C_F}\right)\left(1 + c^2 + 8\hat{m}^2 - \frac{32\hat{m}^4}{1-c^2}\right) \tag{B.2}$$

with

$$\hat{m}^2 = m_t^2/\hat{s}, \qquad \beta = \sqrt{1 - 4\hat{m}^2}, \qquad c = \beta cos\hat{\theta}. \tag{B.3}$$

and where $T_F = 1/2$ and $C_F = 4/3$.

For the asymmetric contribution, the hard gluon radiation process

$$q(p_1) + \bar{q}(p_2) \rightarrow t(p_3) + \bar{t}(p_4) + g(p_5), \tag{B.4}$$

the differential cross section is given by

$$\frac{d\hat{\sigma}_A^{q\bar{q},hard}}{d\Omega dy_{45}dy_{35}} = \frac{\alpha_s^3}{4\pi\hat{s}} \frac{d_{abc}^2}{16N_C^2} \frac{1}{y_{12} \, (y_{34} + 2\hat{m}^2) \, y_{35}}$$
$$\times \left\{ \frac{y_{13}}{y_{15}} \left(y_{13}^2 + y_{14}^2 + y_{23}^2 + y_{24}^2 + 2\hat{m}^2(y_{34} + 2\hat{m}^2 + y_{12}) \right) + 4\hat{m}^2 \, y_{24} \right\}$$
$$- (1 \leftrightarrow 2) - (3 \leftrightarrow 4) + (1 \leftrightarrow 2, 3 \leftrightarrow 4), \tag{B.5}$$

with $N_C = 3$ and $d_{abc}^2 = 40/3$. Quantities are scale up by the partonic center of mass energy $\hat{s}$.

$$p_i = \sqrt{\hat{s}} \, \hat{p}_i, \qquad y_{ij} = 2\hat{p}_i \cdot \hat{p}_j. \tag{B.6}$$

The asymmetric differential cross section for soft plus virtual correction is by

$$\frac{d\hat{\sigma}_A^{q\bar{q},virt+soft}}{d\Omega dy_{45}dy_{35}} = \frac{\alpha_s^3}{2\hat{s}} \frac{d_{abc}^2}{16N_C} \beta \left\{ B(c) - B(-c) \right.$$
$$\left. + (1 + c^2 + 4\hat{m}^2) \left[4\ln\left(\frac{1-c}{1+c}\right) \ln(2w) + D(c) - D(-c) \right] \right\} \tag{B.7}$$

where $w = E_{cut}/\sqrt{\hat{s}}$ and functions $B(c)$ and $D(c)$ defined as

$$B(c) = \frac{1 - c^2 - 8\hat{m}^2}{1 - c^2 - 2\hat{m}^2} \ln\left(\frac{1-c}{2}\right) + (c + 2\hat{m}^2) \left[2Li_2\left(1 - \frac{2m^2}{1-c}\right) - \ln^2\left(\frac{1-c}{2}\right) \right]$$
$$+ \frac{4c}{\beta^2} \frac{2 - c^2 - 7\hat{m}^2}{(1 - 2\hat{m}^2)^2 - c^2} m^2 \, \ln(m^2) + \frac{c}{2} \ln^2(\hat{m}^2)$$
$$- \frac{c}{2\beta^3}(1 - 8\hat{m}^2 + 8\hat{m}^4) \left[\ln^2\left(\frac{1-\beta}{1+\beta}\right) + 4Li_2\left(-\frac{1-\beta}{1+\beta}\right) + \frac{\pi^2}{3} \right] - c\frac{\pi^2}{6}, \tag{B.8}$$

$$D(c) = 2Re\left\{ Li_2\left(\frac{-x}{1-y}\right) - Li_2\left(\frac{1-x}{1-y}\right) - Li_2\left(\frac{1+x}{y}\right) + Li_2\left(\frac{x}{y}\right) \right\}$$
$$+ \ln^2\left|\frac{y}{1-y}\right| - Re \, Li_2(x^2) + \frac{1}{2}\ln^2(x^2) - \ln(x^2)\ln(1 - x^2), \tag{B.9}$$

where

$$x\frac{1-c}{\sqrt{2(1-c-2\hat{m}^2)}}, \qquad y = \frac{1}{2}\left(1-\beta+\sqrt{2(1-c-2\hat{m}^2)}\right), \qquad \text{(B.10)}$$

and Li_2 is the dilogarithm. Note that in python 2.7 the dilogarithm is defined differently.

For the asymmetric quark-gluon scattering process

$$q(p_1) + g(p_2) \rightarrow t(p_3) + \bar{t}(p_4) + q(p_5), \qquad \text{(B.11)}$$

the differential cross section is given by

$$\frac{d\hat{\sigma}_A^{q\bar{q},hard}}{d\Omega dy_{45}dy_{35}} = \frac{\alpha_s^3}{4\pi\hat{s}}\frac{d_{abc}^2}{16N_C(N_C^2-1)}\frac{1}{y_{15}\,(y_{34}+2\hat{m}^2)\,y_{23}}$$

$$\times \left\{\left(\frac{y_{13}}{y_{12}}-\frac{y_{35}}{y_{25}}\right)\left(y_{13}^2+y_{14}^2+y_{35}^2+y_{45}^2+2\hat{m}^2(y_{34}+2\hat{m}^2+y_{15})\right)\right.$$

$$\left. + 4\hat{m}^2\,(y_{45}+y_{14})\right\} - (3 \leftrightarrow 4), \qquad \text{(B.12)}$$

C Parametrising the Phase Space

Here, we show the steps for parameterising the 3-body phase space for the hard process shown in B.5 under the restriction $E_5 > E_{cut}$. As mentioned in section 3.3, we set up four-vectors under the constraints in Equation (21) and find a suitable configuration is given by

$$\hat{p}_1 = \frac{1}{2}(1, sin\theta cos\phi, sin\theta sin\phi, cos\theta)$$

$$\hat{p}_2 = \frac{1}{2}(1, -sin\theta cos\phi, -sin\theta sin\phi, -cos\theta)$$

$$\hat{p}_3 = (E_3, 0, 0, k_3)$$

$$\hat{p}_4 = (1 - E_3 - E_5, -E_5 sin\alpha, 0, -k3 + E_5 cos\alpha)$$

$$\hat{p}_5 = E_5(1, sin\alpha, 0, -cos\alpha) \qquad \text{(C.1)}$$

Four-momentum conservation is used to define invariants in terms of phase-space integration variables. For example from

$$\hat{p}_1 + \hat{p}_2 = \hat{p}_3 + \hat{p}_4 + \hat{p}_5, \qquad \text{(C.2)}$$

One can rearrange and square both sides

$$(\hat{p}_1 + \hat{p}_2 - \hat{p}_3)^2 = (\hat{p}_4 + \hat{p}_5)^2. \tag{C.3}$$

Next, expand the brackets

$$(\hat{p}_1 + \hat{p}_2)^2 + \hat{p}_3^2 + 2\hat{p}_3 \cdot (\hat{p}_1 + \hat{p}_2) = \hat{p}_4^2 + \hat{p}_5^2 + 2\hat{p}_4 \cdot \hat{p}_5 \tag{C.4}$$

Using the the constraints, we see that

$$1 - 2E_3 = y_{45}$$
$$\Rightarrow E_3 = \frac{1 - y_{45}}{2} \tag{C.5}$$

Using a similar procedure, following invariants may be defined using the phase-space integration variables:

$$E_3 = \frac{1 - y_{45}}{2}, \qquad k_3 = \sqrt{E_3^2 - \hat{m}^2}, \qquad E_5 = \frac{y_{35} + y_{45}}{2} \qquad cos\alpha = \frac{\frac{y_{35}}{y_{35}+y_{45}} - E_3}{k3}. \tag{C.6}$$

Other invariants include

$$y_{12} = 1, \qquad y_{13} = E_3 - k_3 cos\theta, \qquad y_{23} = E_3 + k_3 cos\theta$$
$$y_{34} = 1 - y_{35} - y_{45} - 2\hat{m}^2$$
$$y_{15} = E_5(1 - sin\theta cos\phi sin\alpha + cos\theta cos\alpha)$$
$$y_{25} = E_5(1 - sin\theta cos\phi sin\alpha + cos\theta cos\alpha) = 2E_5 - y_{15}$$
$$y_{14} = 1 - y_{13} - y_{15}$$
$$y_{24} = 1 - y_{23} - y_{25} \tag{C.7}$$

The integration limits can now be calculated. For the angles, the limits are trivially given by

$$-1 \le cos\theta \le 1$$
$$0 \le \phi \le 2\pi$$
$$-1 \le cos\alpha \le 1 \tag{C.8}$$

From $-1 \le cos\alpha \le 1$, the y_{35} integration limits is found to be

$$\frac{E_3 - k_3}{(1 - E_3 + k_3)} y_{45} \le \ y_{35} \ \le \frac{E_3 + k_3}{(1 - E_3 - k_3)} y_{45}, \tag{C.9}$$

and from our invariants we see that

$$1 - y_{45} = 2E_3 \geq 2\hat{m}$$

$$\Rightarrow\; y_{45} \leq 1 - 2\hat{m} \tag{C.10}$$

and

$$y_{35} + y_{45} = 2E_5 \geq w$$

$$\Rightarrow\; y_{45} \geq w(1 - \beta), \tag{C.11}$$

hence

$$w(1 - \beta) \leq y_{45} \leq 1 - 2\hat{m} \tag{C.12}$$

Using the parameterisations, y_t and $y_{\bar{t}}$ can be defined in the lab frame as

$$y_t^{lab} = \frac{1}{2}\ln\left(\frac{x_1}{x_2}\right) + \frac{1}{2}\ln\left(\frac{E_3 + k_3 cos\theta}{E_3 - k_3 cos\theta}\right) \tag{C.13}$$

$$y_{\bar{t}}^{lab} = \frac{1}{2}\ln\left(\frac{x_1}{x_2}\right) + \frac{1}{2}\ln\left(\frac{E_4 + k_{4z}}{E_4 - k_{4z}}\right) \tag{C.14}$$

where x_1 and x_2 are the momentum fractions of the colliding partons and E_4 is the energy of the antitop quark given by $1 - E_3 - E_5$. The momentum of the antitop in the z-axis is given by

$$k_{4z} = \vec{k}_4 \cdot \vec{p}_1 = -E_5 sin\alpha cos\phi sin\theta + (-k_3 + E_5 cos\alpha)cos\theta \tag{C.15}$$